Vol. 6 • No. 24 • December 21 • 2016
www.advenergymat.de

ADVANCED ENERGY MATERIALS

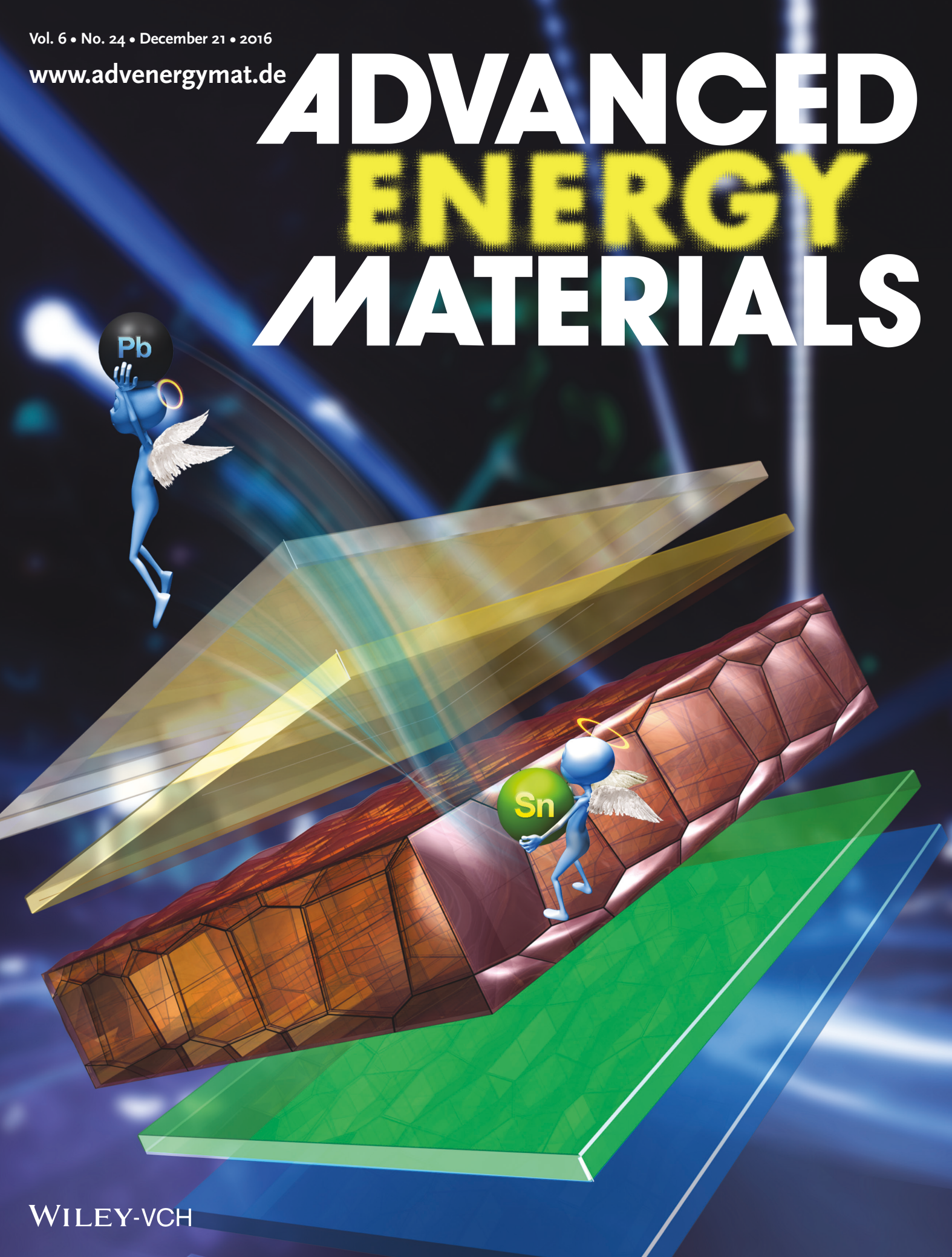

WILEY-VCH

ADVANCED ENERGY MATERIALS
www.advenergymat.de

Heterojunction-Depleted Lead-Free Perovskite Solar Cells with Coarse-Grained B-γ-$CsSnI_3$ Thin Films

Ning Wang, Yuanyuan Zhou, Ming-Gang Ju, Hector F. Garces, Tao Ding, Shuping Pang, Xiao Cheng Zeng, Nitin P. Padture,* and Xiao Wei Sun**

Perovskite solar cells (PSCs) have been emerging as a breakthrough photovoltaic technology, holding unprecedented promise for low-cost, high-efficiency renewable electricity generation. However, potential toxicity associated with the state-of-the-art lead-containing PSCs has become a major concern. The past research in the development of lead-free PSCs has met with mixed success. Herein, the promise of coarse-grained B-γ-$CsSnI_3$ perovskite thin films as light absorber for efficient lead-free PSCs is demonstrated. Thermally-driven solid-state coarsening of B-γ-$CsSnI_3$ perovskite grains employed here is accompanied by an increase of tin-vacancy concentration in their crystal structure, as supported by first-principles calculations. The optimal device architecture for the efficient photovoltaic operation of these B-γ-$CsSnI_3$ thin films is identified through exploration of several device architectures. Via modulation of the B-γ-$CsSnI_3$ grain coarsening, together with the use of the optimal PSC architecture, planar heterojunction-depleted B-γ-$CsSnI_3$ PSCs with power conversion efficiency up to 3.31% are achieved without the use of any additives. The demonstrated strategies provide guidelines and prospects for developing future high-performance lead-free PVs.

1. Introduction

The unprecedented promise of high power conversion efficiency (PCE) and low-cost photovoltaics (PVs) has been the motivation behind the enormous interest in perovskite solar cells (PSCs).[1–6] Halide perovskite materials that are adopted as light absorbers in PSCs have outstanding optoelectronic properties, such as high absorption coefficient, long-range charge diffusion lengths, low exciton binding energies, high carrier mobilities, and suitable bandgaps.[1–4] Halide perovskites are a family of materials with chemical formula ABX_3, where A is a monovalent cation, B is a divalent metal cation, and X is a halide anion. To date, most studies have focused on using hybrid organic-inorganic halide perovskites, in particular methylammonium lead triiodide ($MAPbI_3$) and formamidinium lead triiodide ($FAPbI_3$), as light absorbers in PSCs, where high PCEs have been achieved through the optimization of cell architectures and structures of the perovskite absorber layers.[1–6] However, there are some intrinsic issues associated with the use of the $MAPbI_3$ or $FAPbI_3$ perovskite. First, a large portion (≈35 wt%) of the $MAPbI_3$ or $FAPbI_3$ is lead (Pb). The use of lead-containing substances in electronic devices is severely restricted by the European Union and other countries, motivating the development of lead-free PSCs.[2,6] One of the most feasible replacements for Pb in the perovskite structure is its elemental analog — tin (Sn), and, thus, $MASnI_3$[7] and $FASnI_3$[8] have been studied in PSC applications. Second, it has been suggested that the fragmentation of the organic component (e.g., MA^+ or FA^+) in those hybrid perovskites may make them intrinsically unstable for long-term outdoor applications of PSCs.[9,10] Several recent studies have revealed that the substitution of the organic cation by cesium (Cs) in the perovskite structure significantly enhances the thermal stability.[11,12] In this context, the studies by Chung et al.[13,14] and some of us[15] have showed that the all-inorganic $CsSnI_3$ perovskite has a melting point of 451 °C, and it can be synthesized via melting-solidification, implying superior intrinsic thermal stability. By contrast, the halide perovskite analogs of $MASnI_3$ and $FASnI_3$ perovskites start to decompose at ≈200 °C.[16] The aforementioned considerations provide the rationale for the investigation of $CsSnI_3$ material as a promising thermally stable, lead-free perovskite for next generation PSCs.

Dr. N. Wang, T. Ding, Prof. X. W. Sun
Luminous! Centre of Excellence for Semiconductor Lighting and Displays
School of Electrical and Electronic Engineering
Nanyang Technological University
50 Nanyang Avenue, 639798, Singapore
E-mail: exwsun@hotmail.com

Dr. Y. Zhou, Dr. H. F. Garces, Prof. N. P. Padture
School of Engineering
Brown University
Providence, RI 02912, USA
E-mail: yuanyuan_zhou@brown.edu; nitin_padture@brown.edu

Dr. M.-G. Ju, Prof. X. C. Zeng
Department of Chemistry
University of Nebraska-Lincoln
NE 68588, USA

Dr. S. Pang
Qingdao Institute of Bioenergy and Bioprocess Technology
Chinese Academy of Sciences
Qingdao 266101, P. R. China

Prof. X. W. Sun
Department of Electrical and Electronic Engineering
College of Engineering
South University of Science and Technology of China
Shenzhen 518055, P. R. China

DOI: 10.1002/aenm.201601130

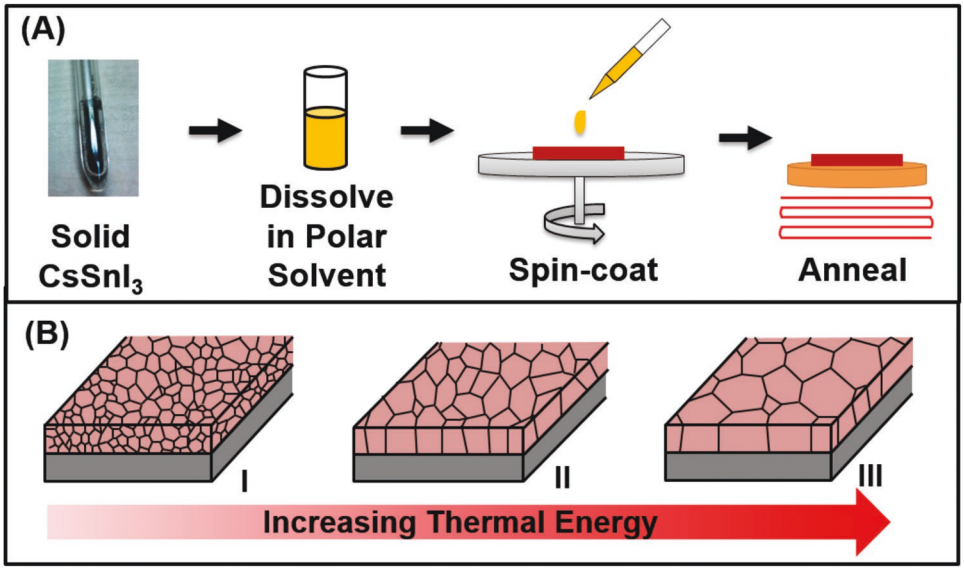

Figure 1. A) Schematic representation of the one-step solution fabrication of B-γ-$CsSnI_3$ thin films. B) Schematic representation of the grain-coarsening driven morphology evolution of as-deposited B-γ-$CsSnI_3$ thin film with increasing heat-treatment temperature.

$CsSnI_3$ has two polymorphs at cell-operating temperatures (20–100 °C): the desirable 'black' B-γ-$CsSnI_3$ phase and the undesirable 'yellow' Y-$CsSnI_3$ phase in the context of solar cell application.[13] The B-γ-$CsSnI_3$ phase has been studied comprehensively, and it has been shown to possess favorable properties for solar cell application. These include a direct band gap of ≈1.3 eV,[13,14] high optical absorption coefficient (≈10^4 cm^{-1}),[17] low exciton binding energy (10–20 meV),[18] and high charge-carrier mobility (up to ≈585 cm^2 V^{-1} s^{-1} for holes).[13] However, there have been only a handful of reports that have used B-γ-$CsSnI_3$ as light absorber in solar cells, but with mixed success,[19–21] highlighting the challenges involved in the development of B-γ-$CsSnI_3$ based PSCs. First, the quality (purity, microstructural morphology, etc.) of the as-fabricated B-γ-$CsSnI_3$ absorber layer has been rarely assessed in the literature. In particular, solution crystallization of B-γ-$CsSnI_3$ can be sensitive to the preparation methods/conditions,[13,15,21] and it can be accompanied by the formation of the undesirable Y-$CsSnI_3$ polymorph,[13] and its degradation product Cs_2SnI_6.[22,23] Second, Sn vacancies (V_{Sn}) exhibit intrinsic low formation-energies in the B-γ-$CsSnI_3$ structure, resulting in 'metallic' B-γ-$CsSnI_3$.[13] Thus, the control of V_{Sn} concentration in the structure for the operation of the B-γ-$CsSnI_3$ in PSCs has been suggested as being critical.[19] Third, there is a paucity of studies in the literature about the understanding of the physics of B-γ-$CsSnI_3$-based solar cell devices. To address these challenges, in this work we have developed a simple solution-deposition-based method to make uniform, coarse-grained B-γ-$CsSnI_3$ thin films, and at the same time explored different feasible solar cell architectures to enhance the performance of B-γ-$CsSnI_3$-based PSCs. As a result, a novel heterojunction-depleted PSC, employing the as-fabricated phase-pure, coarse-grained B-γ-$CsSnI_3$ thin film, is demonstrated with PCE up to 3.31%.

2. Results and Discussion

The solution deposition of B-γ-$CsSnI_3$ thin films is based on the classic 'one-step' spin-coating process, as illustrated in **Figure 1**A. A 20 wt% precursor solution was prepared by dissolving in-house prepared high quality B-γ-$CsSnI_3$ feedstock (using a method reported elsewhere[15]) in a mixed polar solvent. The solution was then spin-coated on the substrate at 6000 rpm for 20 s. A dark-brown, smooth solid thin film gradually evolved during the spinning process. The cross-sectional scanning electron microscope (SEM) micrograph in Figure S1 (Supporting Information) shows that a full-coverage B-γ-$CsSnI_3$ film of ≈120 nm thickness forms on the substrate. This could be the result of rapid nucleation and growth of B-γ-$CsSnI_3$ induced by the supersaturation of the precursor solution by rapid evaporation and/or centrifugal force.[24] The as-formed B-γ-$CsSnI_3$ thin film from the room-temperature (RT) solution crystallization process is expected to exhibit a fine-grain structure, similar to RT-crystallized hybrid perovskites.[24–27] Since B-γ-$CsSnI_3$ is expected to be thermally stable compared to hybrid perovskites,[5] the as-deposited films were subsequently post-annealed at different temperatures over a relatively wide range (100, 150, 200, 250, and 300 °C) for 2 min to coarsen the grains. As depicted in Figure 1B, the as-crystallized polycrystalline B-γ-$CsSnI_3$ thin films (Film I in Figure 1B) after spin-coating are expected to contain fine grains. With increasing temperature, the grains are expected to coarsen and span the film thickness in the final B-γ-$CsSnI_3$ thin films (Films II and III in Figure 1B).[24,28]

Figure 2A–F is top-view SEM micrographs showing the microstructures of B-γ-$CsSnI_3$ thin films without annealing, and those annealed at different annealing temperatures (100, 150, 200, 250, and 300 °C). The coarsening of the grains with increasing annealing temperature is clearly observed. The average grain sizes were determined by image analysis using at

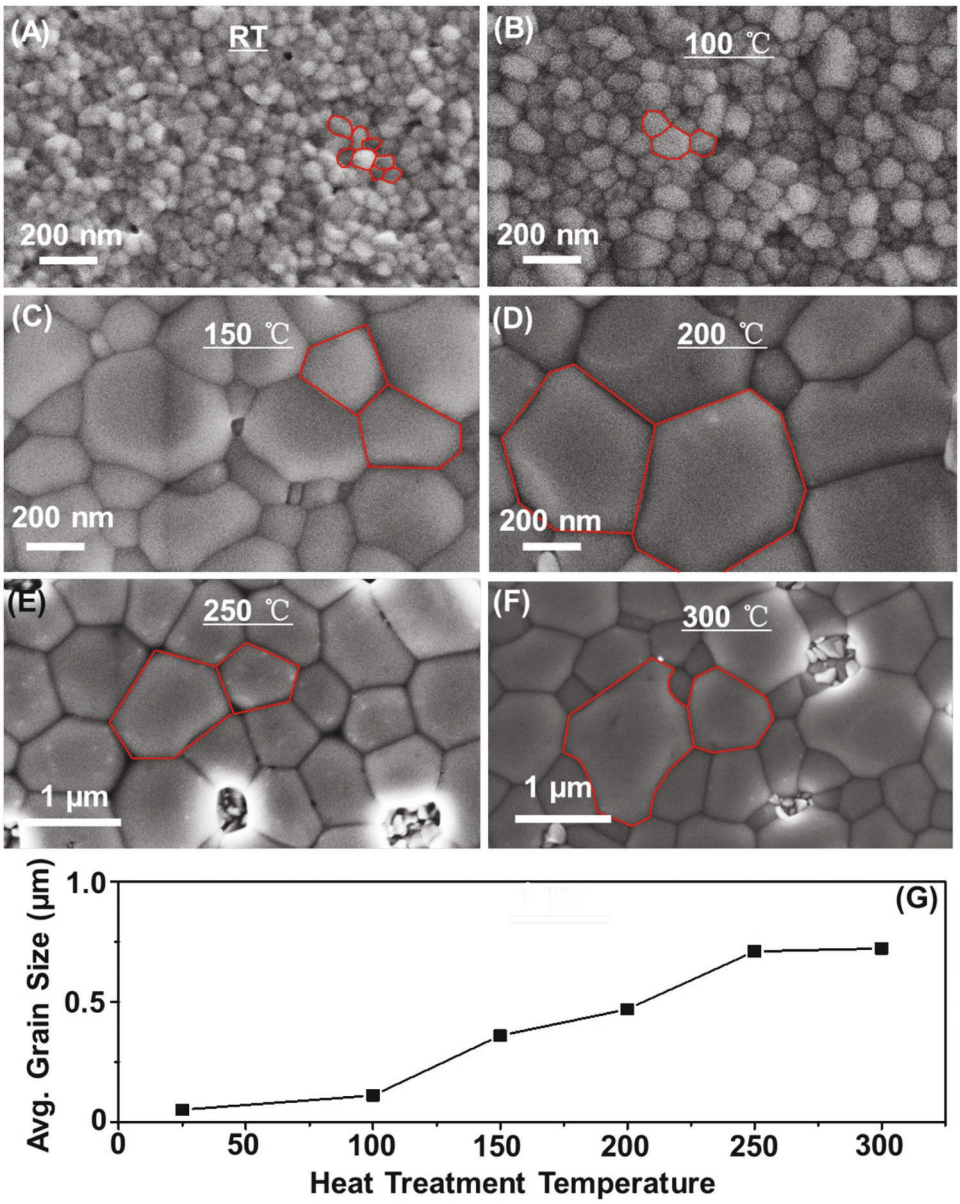

Figure 2. SEM micrographs (top view) of the B-γ-$CsSnI_3$ thin films annealed at different temperatures for 2 min. A) as-deposited, B) 100 °C, C) 150 °C, D) 200 °C, E) 250 °C, and F) 300 °C. G) Average grain size of the B-γ-$CsSnI_3$ thin films with increasing annealing temperature.

least 50 grains per measurement, which are plotted in Figure 2G. (The grain size distributions in each film are reported in Figures S3, Supporting Information.) The as-deposited B-γ-$CsSnI_3$ thin film is composed of nanoscaled 'grains.' The apparent average size of the grains is ≈50 nm, but the 'grains' may contain even smaller subgrains, which are difficult to resolve in the SEM. After annealing at 100 °C, the average grain size increases to ≈100 nm. When the annealing temperature is elevated to 150 °C, flat polygonal grains with triple junction grain boundaries become a predominant microstructural feature in the films, showing close-packing of B-γ-$CsSnI_3$ grains with ≈350 nm size. Such feature becomes even more evident with further increase in the annealing temperatures (200 and 250 °C), where the average grain size reaches ≈720 nm after annealing at 250 °C. The grain coarsening appears to stall beyond this annealing temperature, which may be restricted by the vertical dimension of the film.[29] Meanwhile, some of curved grain edges are developed, which is presumably related to the preferential structural reconstruction of B-γ-$CsSnI_3$ at such high annealing temperature. Overall, more pronounced grain-boundary grooves are observed with increasing annealing temperature, which is the result of preferential diffusion of matter away from the region where the grain boundaries intersect the surface (so-called 'solid-state dewetting').[30] These features do increase the roughness of the films (see the atomic force microscope roughness measurement results in Figure S4, Supporting Information). While those films annealed below 200 °C show nearly full coverage (see lower-magnification SEM images in Figure S2,

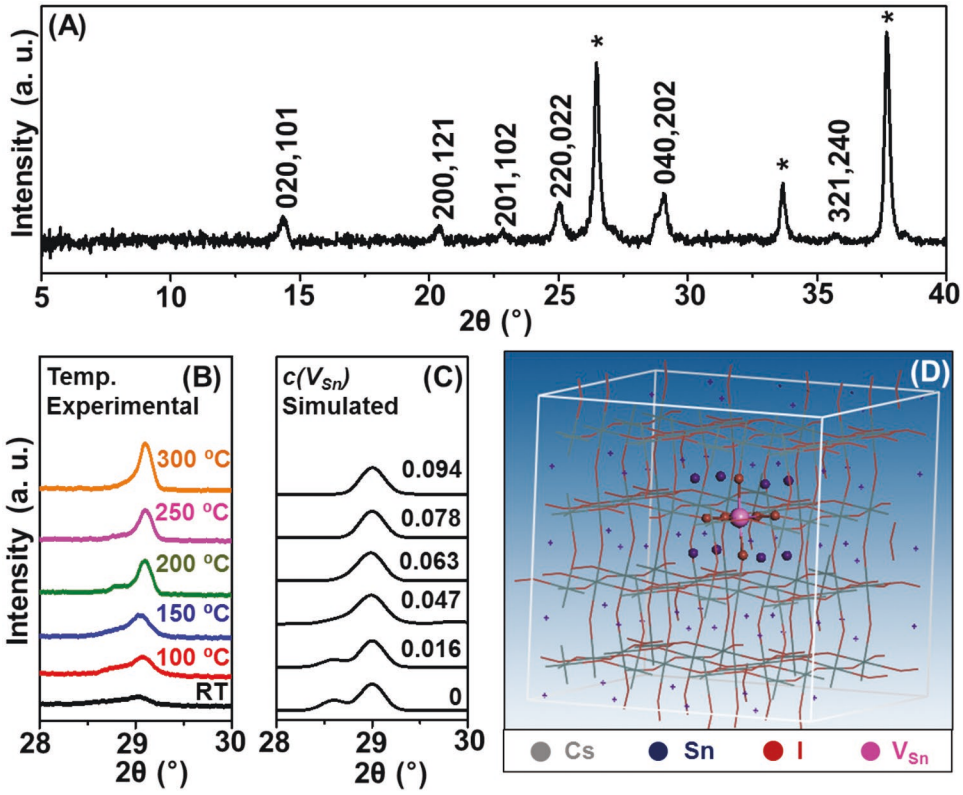

Figure 3. A) Experimental XRD pattern of as-deposited B-γ-$CsSnI_3$ perovskite thin film. B) Experimental XRD patterns (in 28°–30° 2θ range) of B-γ-$CsSnI_3$ perovskite thin film annealed at different temperatures (2 min). C) Simulated XRD patterns of B-γ-$CsSnI_3$ perovskite thin film with different Sn vacancies in the crystal structure. D) Schematic illustration of the crystal structure of B-γ-$CsSnI_3$ containing Sn vacancies.

Supporting Information), microdefects (e.g., pinholes) become more numerous with increasing annealing temperature beyond 200 °C, as shown in Figure 2E–F. Since the film thickness is ≈120 nm, the grain coarsening in these films is essentially 2D, where the substrate and the grain-boundary grooves can play important roles.[24,29]

Figure 3A shows indexed X-ray diffraction (XRD) pattern of the as-spin-coated B-γ-$CsSnI_3$ perovskite thin film. The phase purity of the B-γ-$CsSnI_3$ perovskite is confirmed. Due to the nanoscale nature of the as-crystallized B-γ-$CsSnI_3$ thin films, the 040 and 202 reflections are broadened and appear to overlap. Fit of the XRD pattern (in Figure S5A, Supporting Information) shows a full width at half maximum of 0.33° for the 202 reflection. Using the Scherer equation,[31] the average grain size is estimated at ≈30 nm, which is consistent with the SEM observations and also our previous report on room-temperature solution crystallization of B-γ-$CsSnI_3$.[15] With increasing annealing temperature, the XRD peaks become more intense, which indicates the increase of the crystallinity of the B-γ-$CsSnI_3$ phases. This is consistent with the SEM observation in Figure 2. Note that the grain sizes (>100 nm) of the films annealed at 100, 150, 200, 250, and 300 °C are beyond the validity of the Scherer equation for reliable estimation of the grain size. It is also interesting that there are noticeable changes in diffraction peak characteristics besides the intensities. It is apparent that the ratio of intensities of 202 and 040 peaks decreases with increasing annealing temperature (Figures S5 and S6, Supporting Information). A plausible explanation for this observation is as follows. The relative intensities of the XRD peaks are obtained using the equation $I = |F|^2 p\left(\frac{1+\cos^2 2\theta}{\sin^2\theta\cos\theta}\right)$, where F is the structure factor and p is the multiplicity factor.[32] Considering the low formation energy of Sn vacancies (V_{Sn}),[13] we hypothesize that the propensity for the formation of V_{Sn} increases with increasing annealing temperatures, which is expected to result in a change in the multiplicity factor p. However, since there is no second-phase formation, F is expected to change only negligibly. In order to support this hypothesis, density function theory (DFT) calculations were performed. B-γ-$CsSnI_3$ crystal models with different V_{Sn} concentrations, $c(V_{Sn})$, were built (see Figure 3D). The modeling results confirm that the generation of V_{Sn} in the crystal structure does not result in the formation of new second phases, and, thus, the small change in F is confirmed to have a negligible effect on the calculated XRD intensities. The theoretically calculated XRD patterns for B-γ-$CsSnI_3$ with different $c(V_{Sn})$ are plotted in Figure 3C. Analogous to the effect of increasing annealing temperature on the experimental XRD patterns in Figure 3B, when $c(V_{Sn})$ increases, the frontal peak (at $2\theta = 28.6°$) vanishes gradually, and the overall pattern in the range 2θ 28.0° to 30.0° evolves with a single-peak characteristic. This result is consistent with, and supports, the hypothesis that the annealing temperature affects not only the grain morphology of the thin films but also $c(V_{Sn})$ in the B-γ-$CsSnI_3$ thin films. This is in fact in good agreement with the results reported by Chung et al.[13] where

they suggest that higher heat-treatment temperature activates the generation of V_{Sn} and results in the continuous increase in the 'metallicity' of B-γ-$CsSnI_3$.[13]

Since there is a dearth of studies on B-γ-$CsSnI_3$-based PSCs, different PSC architectures, which are typically employed in the context of hybrid perovskite absorbers,[1] are explored with B-γ-$CsSnI_3$ as the light-absorbing material. The device structure exploration 'roadmap' is shown in **Figure 4**A. Initially, the regular mesoscopic-solar-cell architecture (device structure I) is adopted. Thin films of mesoporous TiO_2 (with compact TiO_2 blocking layer underneath) and Spiro-OMeTAD molecules are used as electron-transporting layer (ETL) and hole-transporting layer (HTL), respectively. (The corresponding energy level alignment diagram is shown in Figure 4B.) The B-γ-$CsSnI_3$ layer is deposited using the 'one-step' solution process followed by annealing at 100 °C, as described above. Almost null photovoltaic response is observed in such B-γ-$CsSnI_3$-based PSC (device structure I), as seen in Figure 4C. In this context, insulating mesoporous Al_2O_3 scaffold is used to replace the mesoporous TiO_2, where a typical mesosuperstructured solar cell (device structure II) is fabricated. As a result, a modest PCE of ≈0.32% is achieved, with short-circuit current density (J_{SC}) of 3.07 mA cm^{-2}, an open-circuit voltage (V_{OC}) of 0.40 V, and a fill factor (*FF*) of 0.261. The enhanced V_{OC} may originate from significantly reduced possibility of direct contact between TiO_2 and Spiro-OMeTAD as a result of the insulating nature of the scaffold. The possible direct contact between TiO_2 and Spiro-OMeTAD can be originated from nonuniform infiltration/coverage of $CsSnI_3$ perovskite upon the mesoporous scaffold as shown in Figure S7 (Supporting Information). Nevertheless, the J_{SC} is still quite low considering the strong absorption characteristic of the narrow-bandgap (≈1.3 eV) B-γ-$CsSnI_3$ perovskite. This indicates that severe recombination must be occurring, which can be attributed to the following. (i) It is possible that the crystallinity of the B-γ-$CsSnI_3$ perovskite is low due to the constrained crystallization environment in the mesopores of the TiO_2 or Al_2O_3 scaffolds,[33,34] which is supported by the careful XRD analysis presented in Figure S8 (Supporting Information). This creates abundant defect states that can serve as recombination centers in the B-γ-$CsSnI_3$ perovskite. (ii) 'One-step' solution-deposited B-γ-$CsSnI_3$ perovskite upon high-surface-area mesoporous scaffolds invariably introduces nonideal solid–solid interfaces between the perovskite and the scaffold material due to the inherent difficulty in controlling the crystallization process and the limitation on the solution concentration that can be used. (iii) We suspect that low-crystallinity impurities, such as Y-$CsSnI_3$ and Cs_2SnI_6, might exist in the as-crystallized B-γ-$CsSnI_3$ thin films upon mesoporous scaffolds, which is under investigation. In order to address these issues, planar heterojunction PSCs (device structure III), in which a phase-pure B-γ-$CsSnI_3$ layer with better crystallinity is employed, resulting in an enhanced PCE of 0.77% (V_{OC} : 0.48 V; J_{SC} : 8.11 mA cm^{-2}; *FF* : 0.198). These results suggest that grain morphology and purity can be the most important factors affecting the performance of B-γ-$CsSnI_3$ in PSCs. However, the planar heterojunction PSC still exhibits a very low *FF*. Considering that the Spiro-OMeTAD layer that is used in this device is undoped, the observed low *FF* is consistent with the *J–V* behavior of PSCs using undoped Spiro-OMeTAD as the HTL reported in the literature.[35] This is primarily due to the low conductivity of undoped Spiro-OMeTAD, which limits the charge transport in the HTL and restricts the corresponding PSC performance. Note that the necessary oxidation step needed to achieve high-performance hole-transporting doped Spiro-OMeTAD layer[36] was not performed here because that heat-treatment invariably degrades the B-γ-$CsSnI_3$ perovskite.

To overcome these issues with the use of Spiro-OMeTAD in the B-γ-$CsSnI_3$-based PSCs, a compact *p*-type nickel oxide (NiO_x)

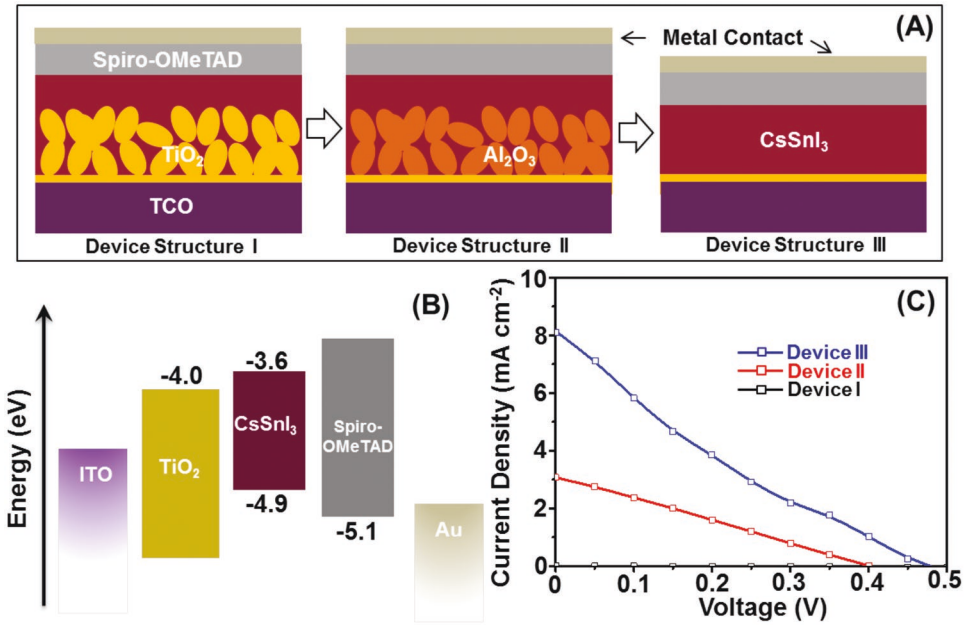

Figure 4. A) Solar cell device architecture 'roadmap' for using B-γ-$CsSnI_3$ as light absorber, and B) energy level diagram of device used in this work. C) *J–V* responses from the corresponding devices. The *J–V* performance parameters extracted from (C) are included in Table S1 (Supporting Information).

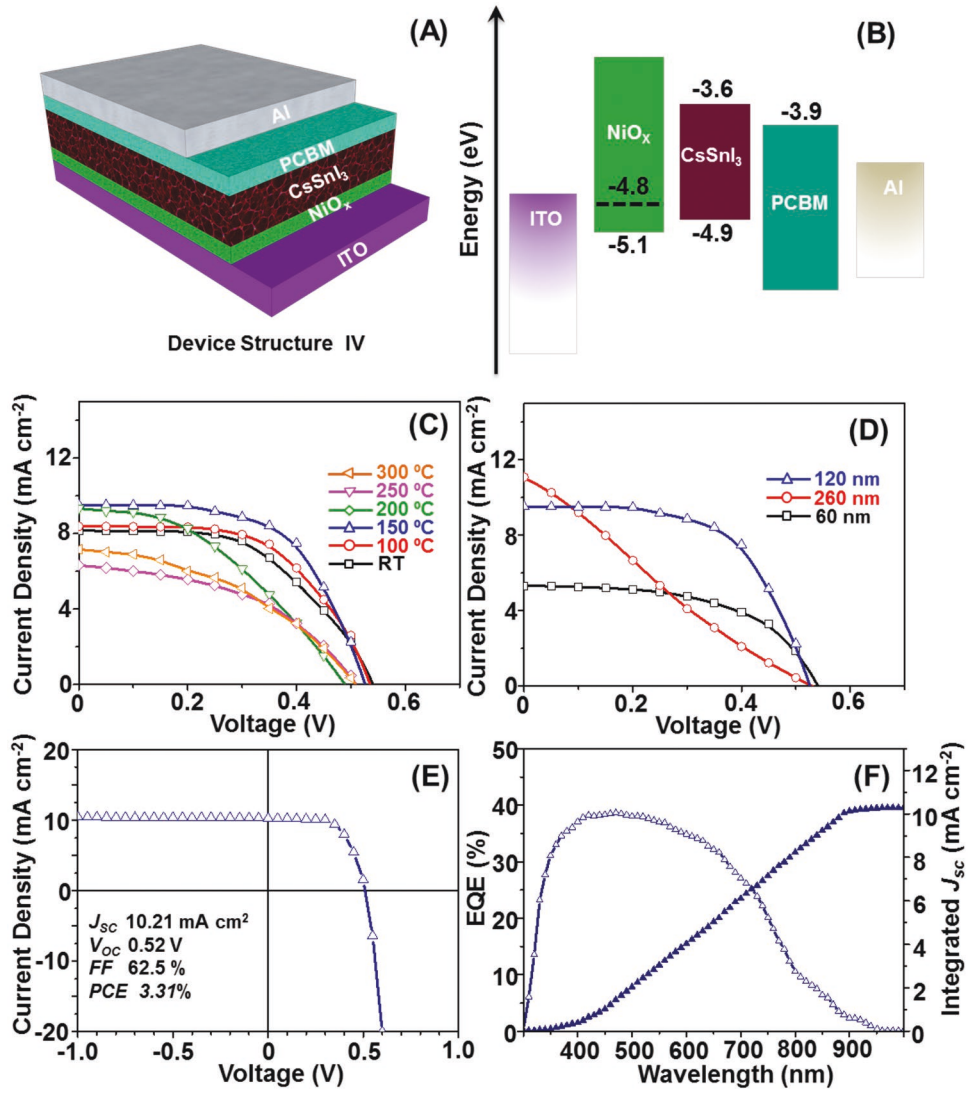

Figure 5. A) Scheme of the 'inverted' structure planar B-γ-$CsSnI_3$ PSC device employing NiO_x as HTL and PCBM as ETL, and B) corresponding energy level diagram (the dashed line indicates NiO_x work function). *J–V* performance of 'inverted' planar PSCs with B-γ-$CsSnI_3$ thin films under standard AM 1.5G one sun illumination: C) annealed at different temperatures and D) different film thicknesses. E) *J–V* performance of the 'champion' B-γ-$CsSnI_3$ PSC (150 °C film annealing temperature, ≈120 nm film thickness), and F) the corresponding EQE spectrum. The *J–V* performance parameters extracted from the (C), (D), and (E) are included in Table S1 (Supporting Information).

HTL is employed, and an inverted PSC structure (device structure IV) is adopted with solution-processed phenyl-C61-butyric acid methyl ester (PCBM) serving as the ETL (**Figure 5**A). The deposition procedure of the high-quality pinhole-free NiO_x layer is described in the Supporting Information. A UV–ozone treatment is followed after the NiO_x deposition. The resultant NiO_x layer has a work function of about −4.8 eV (see the energy level alignment of device structure IV in Figure 5B),[37] which is energetically favorable for hole transport. As a result, this device demonstrates a significantly enhanced PCE of 2.61% (V_{OC} : 0.52 V; J_{SC} : 8.39 mA cm^{-2}; *FF* : 0.598). The J_{SC} and *FF* of this NiO_x/perovskite/PCBM device are obviously higher than those of the TiO_2/perovskite/Spiro-OMeTAD device, which is associated with alleviation of the aforementioned HTL issue.

Since the post-annealing condition has an important effect on the microstructural characteristics of the B-γ-$CsSnI_3$ perovskite thin films, the typical *J–V* performances of the PSCs based on the nondeposited and annealed perovskite films are compared in Figure 5C. The optimal PCE of 3.00% (V_{OC} : 0.52 V; J_{SC} : 9.52 mA cm^{-2}; *FF* : 0.606) is achieved in the PSCs based on the film annealed at 150 °C. For the devices fabricated with milder annealing conditions (RT and 100 °C), the PCE values are 2.35% and 2.61%, respectively. The low J_{SC} values of the PSCs with films that are not annealed, or annealed at low temperatures, contribute significantly to their low PCEs. This is consistent with the fact that the abundant grain boundaries contained in these fine-grained B-γ-$CsSnI_3$ thin films can contribute to significant electron-hole recombination. However, an increase in the film annealing temperature results in the notable drop in V_{OC} and J_{SC} values, and only 1.51% PCE (V_{OC} : 0.50 V; J_{SC} : 6.32 mA cm^{-2}; *FF* : 0.478) is reported in the PSCs with annealing temperature of 300 °C.

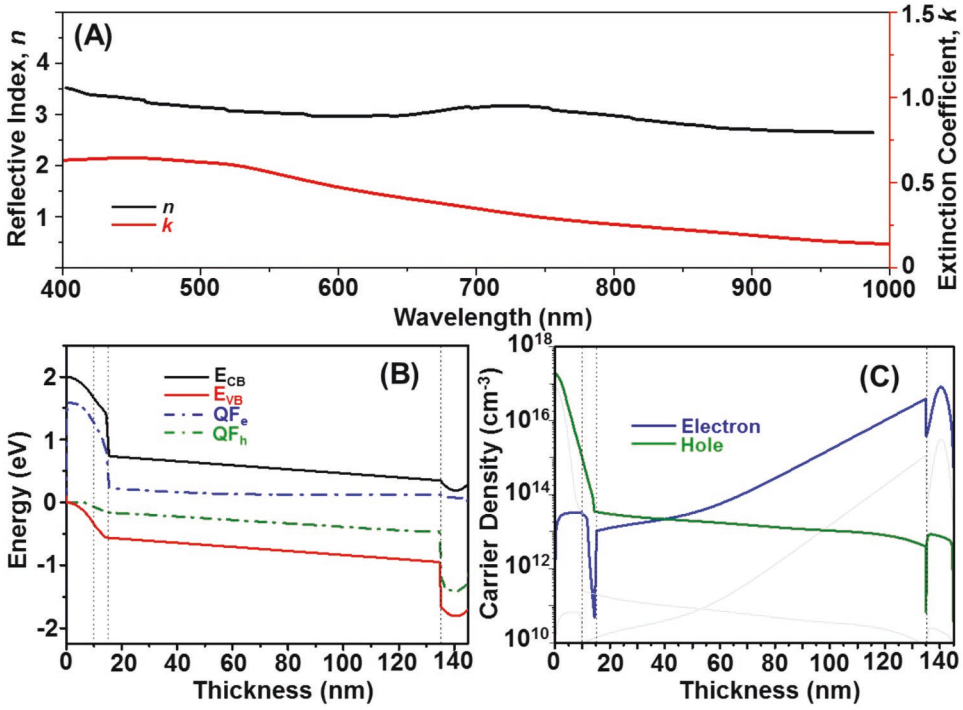

Figure 6. A) Reflective index (n) and extinction coefficient (k) of the B-γ-$CsSnI_3$ thin film sample in the wavelength range 400–1000 nm. B) Simulated band gap characteristics with short-circuit condition across all regions of B-γ-$CsSnI_3$-based PSC under standard AM 1.5G one sun illumination. QF_e, QF_h, E_{CB}, and E_{VB} stand for quasi-Fermi level of electron and hole, and edge-energy of conduction band and valence band, respectively. C) Carrier density profiles of B-γ-$CsSnI_3$-based PSC. The short dashed lines in (B) and (C) indicate the locations of the interfaces in NiO_x/B-γ-$CsSnI_3$/PCBM device.

This may be associated with the following two effects. (i) The roughness of the B-γ-$CsSnI_3$ film increases due to the grain coarsening process, as discussed in the context of Figure 2. (ii) The higher annealing temperatures result in an increase of $c(V_{Sn})$. This has a detrimental effect on the PV performance because the high concentration of holes associated with the high $c(V_{Sn})$ in the B-γ-$CsSnI_3$ reduces the carrier lifetime of the photogenerated electrons, which is particularly unfavorable in the operation of a planar heterojunction solar cell. In this context, a combination of large grain size, high film smoothness, and moderate V_{Sn} generation can be responsible for the best performance of PSCs using the B-γ-$CsSnI_3$ thin films annealed at 150 °C.

The effect of the perovskite film thickness on the PSC performance is further investigated. The results shown in the Figure 5D indicate that the PCE drops when the film thickness is reduced to ≈60 nm or increased to ≈260 nm. While the relatively poorer performance at 60 nm film thickness can be due to the reduced light absorption, the device with thicker films sustains a substantial drop in *FF*, and correspondingly PCE, regardless of the enhanced absorption. The UV–vis absorption spectra of the ≈60, ≈120, and ≈260 nm thick films of B-γ-$CsSnI_3$ are compared in Figure S9 (Supporting Information). These results highlight the critical role of B-γ-$CsSnI_3$ film thickness on the photovoltaic performance. Figure 5E and 5F plots the *J–V* response and the external quantum efficiency (EQE) spectrum, respectively, of the 'champion' PSC based on a coarse-grained B-γ-$CsSnI_3$ thin film annealed at 150 °C. A PCE of 3.31% was achieved with V_{OC} of 0.52 V, J_{SC} of 10.21 mA cm^{-2}, and *FF* of 0.625. These performance parameters are the best to-date in the literature for PSCs employing B-γ-$CsSnI_3$ as the light absorber.[19–21,38] Note that previously reported PCEs of B-γ-$CsSnI_3$-based PSCs without additives are less than 1%.

To understand qualitatively the photovoltaic features in the 'champion' B-γ-$CsSnI_3$-based planar-heterojunction PSC, the optoelectronic simulation of the device using the APSYS software package is performed. First, the optical constants including refractive index (n) and extinction coefficients (k) of the B-γ-$CsSnI_3$ thin film are measured by spectroscopic ellipsometry, combining transmittance, and near-normal incidence reflectance. In **Figure 6**A, the curve of the dimensionless k has a trend similar to that of the optical absorption profile, and the value of n varies from 2.5 to 3.3 in the range wavelength 400–900 nm. Based on the reported parameters as listed in Table S1 (Supporting Information), the band diagram of the device is shown in Figure 6B, where a flat-band condition is reached for efficient photogenerated charge-carrier separation under simulated standard AM 1.5G one-sun (100 mw cm^{-2}) illumination. Also note that the physical parameters in the real device may have some differences. This flat-band characteristic indicates, in this situation, that the B-γ-$CsSnI_3$ absorber layer is fully depleted, which allows efficient charge collection at the ETL/absorber or HTL/absorber interfaces driven by the built-in electrical field. By contrast, for a device employing a thick B-γ-$CsSnI_3$ absorber layer, field-free regions exist, where the charge carriers would tend to recombine. Figure 6C shows the carrier concentration profile in such a device. Our results clearly

indicate that the photoactive region is almost fully depleted, which assists in the conduction of the photogenerated charge carriers to their respective electrodes. Slight asymmetry in carrier concentration is observed owing to the different material-based charge extraction electrodes with asymmetric band alignment in relation to the B-γ-$CsSnI_3$ absorber. Note that the light-induced charge carrier densities for the B-γ-$CsSnI_3$ solar cell are still relatively low, which is consistent with the low J_{SC} obtained in the corresponding *J–V* curves in Figure 5. In this context, further optimization of composition, defects, and microstructural characteristics in the B-γ-$CsSnI_3$ may lead to further enhancements in the performance in the resultant heterojunction-depleted PSCs.

3. Conclusions

We report a simple solution method for the deposition of B-γ-$CsSnI_3$ perovskite thin films, and the controlled coarsening of the grains using different annealing temperatures. Heterojunction-depleted lead-free PSCs using these thin films as light absorber are successfully demonstrated. Here, a NiO_x HTL, with energetically favorable band alignments, is used to resolve the issue of the incompatibility of organic HTL, resulting in PCE as high as 3.31% in this novel PSC structure. Our results indicate that the rational design/control of the solar cell architecture and the B-γ-$CsSnI_3$ perovskite microstructures are important for the further development of high-performance lead-free PSCs.

4. Experimental Section

Synthesis of B-γ-$CsSnI_3$ Materials and Films: The B-γ-$CsSnI_3$ raw material was synthesized by melting it in evacuated tubes. Here, appropriate amounts of SnI_2 (Alfa Aesar, USA) and CsI (Sigma-Ardrich, USA) were mixed and placed in pyrex tubes. The tubes were then evacuated to 1×10^{-6} Torr vacuum and sealed using an oxy-methane torch. The evacuated tubes were then placed in a tube furnace and heated to 550 °C (above the melting point of $CsSnI_3$ of 435 °C) and held for 6 h, followed by slow cooling at a rate of 20 °C h^{-1} to room temperature. The tubes were opened in a glovebox, and the 'black' B-γ-$CsSnI_3$ was added to a mixed polar organic solvent resulting in a clear yellow solution. The solvent consists of a mixture of methoxyactonitrile (Tokyo Chemical, Japan), dimethylformamide (Sigma-Ardrich, USA), and acetonitrile (Fisher Scientific, USA) in 1:3:2 volumetric proportion, respectively. This solution was then used for the solution-processing of B-γ-$CsSnI_3$ perovskite thin films. The thickness of the B-γ-$CsSnI_3$ thin films can be easily adjusted by controlling the solution concentration and the spin-coating conditions. Typically, to obtain B-γ-$CsSnI_3$ thin films with a thickness of ≈120 nm, as-prepared B-γ-$CsSnI_3$ solution with concentration of 20 wt% was spin-coated on the substrate at 6000 rpm for 20 s. The as-deposited B-γ-$CsSnI_3$ thin films were annealed at different temperatures (100, 150, 200, 250, and 300 °C) for 2 min before the next steps.

Characterization: XRD patterns were obtained using Cu K_α radiation (λ = 0.15406 nm) with a step scan of 0.02° on an X-ray diffractometer (Bruker D8-advance, Karlsruhe, Germany). The XRD instrumental broadening was calibrated using LaB_6 standard sample, which was considered in the application of the Scherer equation. The morphologies of thin films were characterized using a scanning electron microscope (SEM; LEO 1530VP, Carl Zeiss, Germany). For the XRD and SEM studies, the substrate used was fluorinated-tin-oxide-coated glass. The local roughness of the thin films was characterized using a conventional atomic force microscope (MFP-3D Origin, Asylum Research, USA). Optical absorption spectra were collected using a UV-Vis-NIR spectrophotometer (UV-1800, Shimadzu, Japan). Photoluminescence spectra were recorded on a fluorescence spectrophotometer (RF-5301PC, Shimadzu, Japan), where the excited wavelength was 600 nm. Reflective index and extinction coefficient were measured using a spectroscopic ellipsometry (VB250, J. A. Woollam, USA). Quartz substrates were used for all the optical measurements.

Device Fabrication and Testing: The prepatterned indium-tin-oxide (ITO)-coated glass substrates (sheet resistance of 15 Ω sq^{-1}, Lumtec, Taiwan) were cleaned ultrasonically with Alconox (detergent) solution, followed by sonication in the sequence: deionized water, acetone, and isopropyl alcohol, for 15 min each, and then the substrates were dried using blowing nitrogen gas. The ITO-coated glass substrates were then UV-ozone treated for 20 min prior to the deposition of the other layers. For the regular-structure solar cells, compact TiO_2 ETL or compact TiO_2/mesoporous TiO_2 or compact TiO_2/mesoporous Al_2O_3 layers were then deposited. (The detailed procedure for deposition of these layers is included in the Supporting Information.) The B-γ-$CsSnI_3$ thin films were then deposited. The B-γ-$CsSnI_3$ solution was heated with continuous stirring at 60 °C overnight in a glovebox (O_2 < 0.5 ppm, H_2O < 0.5 ppm) prior to deposition. Sequentially, a Spiro-OMeTAD HTL was cast by spin-coating its solution (100 mg mL^{-1} in chlorobenzene) at 3000 rpm for 60 s. Note that additives like $Li(CF_3SO_2)_2N$ and 4-tert-butylpyridine (tBP) were not, as noted in the main paper. The device (active area: 3.2 mm × 3.2 mm) was completed by thermal evaporation of the Au electrode (100 nm thickness) on top. For the fabrication of the inverted-structure solar cells, NiO_x layers were deposited on the precleaned ITO-coated glass substrates using the procedures described earlier. The B-γ-$CsSnI_3$ thin films were then deposited, followed by solution casting of a 10 nm thick PCBM layer using a 20 mg mL^{-1} solution of PCBM in 1,2-dichlorobenzene. The spin coating condition used was 4000 rpm for 60 s. A 100 nm Al electrode layer, instead of Au, was deposited to complete the device.

The current density–voltage (*J–V*) of the solar cells were measured using a Keithley 2400 sourcemeter under simulated AM1.5 illumination (100 mW cm^{-2}) by a Xenon-lamp-based solar simulator (Solar Light Co. Inc., USA). The light intensity was calibrated using a Si-reference cell certified by the National Renewable Energy Laboratory, with the mismatch factor less than 2%. A nonreflective mask was used for defining the cell area (0.09 cm^2). The EQE spectra were recorded with an EQE measurement system (PVE 300, Bentham, UK) comprising a Xenon lamp, a momochoromator, a chopper, a lock-in amplifier, and a calibrated silicon photodetector.

DFT Modeling: First principles calculations were performed to understand the structure of B-γ-$CsSnI_3$. These calculations were performed using the projected augmented wave plane-wave basis, implemented in the Vienna ab initio simulation package.[39–41] An energy cutoff of 520 eV is employed and the atomic positions are optimized using the conjugate gradient scheme without any symmetric restrictions until the maximum force on each of them is less than 0.02 eV $Å^{-1}$. The perfect B-γ-$CsSnI_3$ was modeled with 4 × 4 × 4 grid for the *k*-point sampling. The B-γ-$CsSnI_3$ with certain Sn-vacancies was considered with a large super cell, which included a total of 320 atoms. These models containing different Sn-vacancies concentration were modeled with only Γ point for the *k*-point sampling. The generalized gradient approximation exchange-correlation DFT functional Perdew–Burke–Ernzerhof (PBE) with DFT-D3, which includes the dispersion interaction, was employed for the geometrical optimization. The electronic-structure calculations were performed using the PBE functional. Based on the optimized geometries, the XRD was calculated by Reflex module implements in Material Studio.

Self-Consistent Device Simulation: The device physics of the best-performing B-γ-$CsSnI_3$-based PSCs was studied numerically using a commercial simulation package of APSYS. APSYS is able to solve the Poisson's equations, drift-diffusion equations, and the continuity

equations with proper boundary conditions and material parameters set by the user. The Poisson's equations solved in the simulator are as follows

$$-\nabla(\nabla V) = \frac{e}{\varepsilon_s}\left(-n + p + N_D^+ - N_A^-\right)$$

where V is the potential distribution within each semiconductor layer, and n, p, N_D^+, and N_A^- denote the electron concentration, hole concentration, ionized donor concentration, and the ionized acceptor concentration, respectively. The relationship between the current density and the applied voltage is calculated using the following equations

$$J_n = q \cdot \mu_n \cdot n \cdot E + e \cdot D_n \cdot \nabla n$$
$$J_p = q \cdot \mu_p \cdot p \cdot E + e \cdot D_p \cdot \nabla p$$

where, J_n and J_p represent the spatial electron current density and the hole current density, respectively. We use μ_n and μ_p to account for the electron mobility and the hole mobility, respectively, while E represents the applied electric field. D_n and D_p stand for the diffusion constants for electrons and hole, respectively, and they can be calculated according to the well-known Einstein relationship. The current continuity equations employed in this simulator are as follows

$$\nabla \cdot J_n - \sum_j R_n^{tj} - R_{sp} - R_{au} + G_{opt}(t) = \frac{\partial n}{\partial t} + N_D \frac{\partial f_D}{\partial t}$$
$$\nabla \cdot J_p + \sum_j R_p^{tj} + R_{sp} + R_{au} - G_{opt}(t) = -\frac{\partial p}{\partial t} + N_A \frac{\partial f_A}{\partial t}$$

where the electron (n) and hole (p) recombination rate is achieved through the j_{th} deep trap, which are shown by $\sum_j R_n^{tj}$ and $\sum_j R_p^{tj}$. However, in order to simplify the calculations, we treat the deep trap-caused recombination rate by setting a recombination lifetime, such that $\sum_j R_n^{tj} = \frac{n-n_0}{\tau_n}$ and $\sum_j R_p^{tj} = \frac{p-p_0}{\tau_p}$ in which τ_n and τ_p are the trap-caused recombination lifetimes for electrons and holes, respectively. R_{sp} and R_{au} denote the spontaneous recombination rate and Auger recombination rate. $G_{opt}(t)$ represents the carrier generation rate caused by the external influence such as the optical excitation with high energy photons. Here, f_D and f_A mean the occupancy of the donor and acceptor levels, respectively with N_D and N_A denoting the donor and acceptor concentration, respectively.

Supporting Information

Supporting Information is available from the Wiley Online Library or from the author.

Acknowledgements

N.W., T.D., and X.W.S. thank the financial support from the National Research Foundation of Singapore (NRF-CRP11-2012-01). Y.Z., H.F.G., and N.P.P. acknowledge the funding from U.S. National Science Foundation (DMR-1305913 and OIA-1538893). M.-G.J. and X.C.Z. thank the U.S. National Science Foundation (OIA-1538893 and DMR-1420645 (MRSEC)) for the financial support. S.P.P. thanks the financial support from the Youth Innovation Promotion Association of CAS (Grant No. 2015167).

Received: May 29, 2016
Revised: July 28, 2016
Published online:

[1] S. D. Stranks, H. J. Snaith, *Nat. Nanotechnol.* **2015**, *10*, 391.
[2] Y. Zhou, K. Zhu, *ACS Energy Lett.* **2016**, *1*, 64.
[3] M. Gratzel, *Nat. Mater.* **2014**, *13*, 838.
[4] M. Yang, Y. Zhou, Y. Zeng, C.-S. Jiang, N. P. Padture, K. Zhu, *Adv. Mater.* **2015**, *27*, 6363.
[5] Y. Zhou, M. Yang, S. Pang, K. Zhu, N. P. Padture, *J. Am. Chem. Soc.* **2016**, *138*, 5535.
[6] B. V. Lotsch, *Angew. Chem. Int. Ed.* **2014**, *53*, 635.
[7] F. Hao, C. C. Stoumpos, D. H. Cao, R. P. H. Chang, M. G. Kanatzidis, *Nat. Photonics* **2014**, *8*, 489.
[8] T. M. Koh, T. Krishnamoorthy, N. Yantara, C. Shi, W. L. Leong, P. P. Boix, A. C. Grimsdale, S. G. Mhaisalkar, N. Mathews, *J. Mater. Chem. A* **2015**, *3*, 14996.
[9] B. Conings, J. Drijkoningen, N. Gauquelin, A. Babayigit, J. D'Haen, L. D'Olieslaeger, A. Ethirajan, J. Verbeeck, J. Manca, E. Mosconi, F. D. Angelis, H.-G. Boyen, *Adv. Energy Mater.* **2015**, *5*, 1500477.
[10] Y.-Y. Zhang, S. Chen, P. Xu, H. Xiang, X.-G. Gong, A. Walsh, S.-H. Wei, arXiv: 1506.01301.
[11] G. E. Eperon, G. M. Paternò, R. J. Zampetti Sutton, A. A. Haghighirad, F. Cacialli, H. J. Snaith, *J. Mater. Chem. A* **2015**, *3*, 19688.
[12] R. R. Beal, D. J. Slotcavage, T. Leijtens, A. R. Bowring, R. A. Belisle, W. H. Nguyen, G. F. Burkhard, E. T. Hoke, M. D. McGehee, *J. Phys. Chem. Lett.* **2016**, *7*, 746.
[13] I. Chung, J. H. Song, J. Im, J. Androulakis, A. J. Freeman, J. T. Kenney, M. G. Kanatzidis, *J. Am. Chem. Soc.* **2012**, *134*, 8579.
[14] I. Chung, B. Lee, J. He, R. P. H. Chang, M. G. Kanatzidis, *Nature* **2012**, *485*, 486.
[15] Y. Zhou, H. F. Garces, B. S. Senturk, A. L. Ortiz, N. P. Padture, *Mater. Lett.* **2013**, *110*, 127.
[16] Y. Dang, Y. Zhou, X. Liu, D. Ju, S. Xia, H. Xia, X. Tao, *Angew. Chem.* **2016**, *55*, 1.
[17] K. Shum, Z. Chen, J. Qureshi, C. Yu, J. J. Wang, W. Pfenninger, N. Vockic, J. Midgley, J. T. Kenney, *Appl. Phys. Lett.* **2010**, *96*, 221903.
[18] Z. Chen, C. Yu, K. Shum, J. J. Wang, W. Pfenninger, N. Vockic, J. Midgley, J. T. Kenney, *J. Lumin.* **2012**, *132*, 345.
[19] M. H. Kumar, S. Dharani, W. H. Leong, P. P. Boix, R. R. Prabhakar, T. Baikie, C. Shi, H. Ding, R. Ramesh, M. Asta, M. Grätzel, S. G. Mhaisalkar, N. Mathews, *Adv. Mater.* **2014**, *26*, 7122.
[20] Z. Chen, J. J. Wang, Y. Ren, C. Yu, K. Shum, *Appl. Phys. Lett.* **2012**, *101*, 093901.
[21] K. P. Marshall, R. I. Walton, R. A. Hatton, *J. Mater. Chem. A* **2015**, *3*11631.
[22] Z. Xiao, Y. Zhou, H. Hosono, T. Kamiya, *Phys. Chem. Chem. Phys.* **2015**, *17*, 18900.
[23] Z. Xiao, H. Lei, X. Zhang, Y. Zhou, H. Hosono, T. Kamiya, *Bull. Chem. Soc. Jpn.* **2015**, *88*, 1250.
[24] Y. Zhou, O. S. Game, S. Pang, N. P. Padture, *J. Phys. Chem. Lett.* **2015**, *6*, 4827.
[25] Y. Zhou, M. Yang, W. Wu, A. L. Vasiliev, K. Zhu, N. P. Padture, *J. Mater. Chem. A* **2015**, *3*, 8178.
[26] Z. Zhou, Z. Wang, Y. Zhou, S. Pang, D. Wang, H. Xu, Z. Liu, N. P. Padture, G. Cui, *Angew. Chem. Int. Ed.* **2015**, *54*, 9705.
[27] S. Pang, Y. Zhou, Z. Wang, M. Yang, A. R. Krause, Z. Zhou, Z. Kai, N. P. Padture, G. Cui, *J. Am. Chem. Soc.* **2016**, *138*, 750.
[28] W. D. Kingery, H. K. Bowen, D. R. Uhlmann, *Introduction to Ceramics*, 2nd Ed., Wiley Interscience, New York **1976**.
[29] C. V. Thompson, *Annu. Rev. Mater. Sci.* **2010**, *30*, 159.
[30] H. A. Stone, M. J. Aziz, D. Margetis, *J. App. Phys.* **2005**, *97*, 113535.
[31] B. E. Warren, *X-Ray Diffraction*, Addison-Wesley Publishing Co., UK **1969**.
[32] C. Giacovazzo, *Fundamentals of Crystallography*, Oxford University Press, UK **1992**.

[33] Y. Zhou, J. Kwun, H. F. Garces, S. Pang, N. P. Padture, *Chem. Comm.* **2016**, *52*, 7273.
[34] Y. Zhou, A. L. Vasiliev, W. Wu, M. Yang, S. Pang, K. Zhu, N. P. Crystal Padture, *J. Phys. Chem. Lett.* **2015**, *6*, 2292.
[35] M.-C. Jung, S. R. Raga, L. K. Ono, Y. Qi, *Sci. Rep.* **2015**, *5*, 9863.
[36] Y. Zhou, M. Yang, A. L. Vasiliev, H. F. Graces, Y. Zhou, D. Wang, S. Pang, K. Zhu, N. P. Padture, *J. Mater. Chem. A* **2015**, *3*, 9249.
[37] Z. Zhai, X. Huang, M. Xu, J. Yuan, J. Peng, W. Ma, *Adv. Energy Mater.* **2013**, *3*, 1614.
[38] D. Sabba, H. K. Mulmudi, R. R. Prabhakar, T. Krishnamoorthy, T. Baikie, P. P. Boix, S. Mhaisalkar, N. Mathews, *J. Phys. Chem. C* **2015**, *4*, 1763.
[39] G. Kresse, J. Hafner, *Phys. Rev. B* **1993**, *47*, 558.
[40] P. E. Blöchl, *Phys. Rev. B* **1994**, *50*, 17953.
[41] J. P. Perdew, K. Burke, M. Ernzerhof, *Phys. Rev. Lett.* **1996**, *77*, 3865.